This is the Pre-Published Version.
This is the peer reviewed version of the following article: Dai, T., Zhang, X., Sun, M., Huang, B., Zhang, N., Da, P., ... & Yan, C. H. (2021). Uncovering the promotion of CeO2/CoS1. 97 heterostructure with specific spatial architectures on oxygen evolution reaction. Advanced Materials, 33(42), 2102593, which has been published in final form at https://doi.org/10.1002/adma.202102593. This article may be used for non-commercial purposes in accordance with Wiley Terms and Conditions for Use of Self-Archived Versions. This article may not be enhanced, enriched or otherwise transformed into a derivative work, without express permission from Wiley or by statutory rights under applicable legislation. Copyright notices must not be removed, obscured or modified. The article must be linked to Wiley's version of record on Wiley Online Library and any embedding, framing or otherwise making available the article or pages thereof by third parties from platforms, services and websites other than Wiley Online Library must be prohibited.

Uncovering the Promotion of $CeO_2/CoS_{1.97}$ Heterostructure with Specific Spatial Architectures on Oxygen Evolution Reaction

Tengyuan Dai, Xin Zhang, Mingzi Sun, Bolong Huang,* Nan Zhang, Pengfei Da, Rui Yang Zidong He, Wei Wang, Pinxian Xi,* and Chun-Hua Yan

T.Y. Dai, X. Zhang, Prof. B. Huang, N. Zhang, P.F. Da, R. Yang, Z.D. He, W. Wang, Prof. P. Xi, Prof. C.-H. Yan

State Key Laboratory of Applied Organic Chemistry, Frontiers Science Center for Rare Isotopes, College of Chemistry and Chemical Engineering, Lanzhou University, Lanzhou 730000, China

E-mail: xipx@lzu.edu.cn

M. Sun, Prof. B. Huang

Department of Applied Biology and Chemical Technology, The Hong Kong Polytechnic University, Hong Kong SAR, China

E-mail: bhuang@polyu.edu.hk

Prof. C.-H. Yan

Beijing National Laboratory for Molecular Sciences, State Key Laboratory of Rare Earth Materials Chemistry and Applications, PKU-HKU Joint Laboratory in Rare Earth Materials and Bioinorganic Chemistry, Peking University, Beijing 100871, China.

Keywords: heterostructure, spatial architectures, oxygen evolution reaction, surface reconstruction, structure-performance relationships

Structural engineering and compositional controlling have been extensively applied in rationally designing and fabricating advanced freestanding electrocatalysts. The key relationship between the spatial distribution of components and enhanced electrocatalysis performance still needs further elaborate elucidation. Here, we construct CeO_2 substrate supported $CoS_{1.97}$ (CeO_2-$CoS_{1.97}$) and $CoS_{1.97}$ with CeO_2 surface decorated ($CoS_{1.97}$-CeO_2) materials to comprehensively investigate the origin of spatial architectures for the oxygen

evolution reaction (OER). CeO_2-$CoS_{1.97}$ exhibits a low overpotential of 264 mV at 10 mA cm^{-2} due to the stable heterostructure and faster mass transfer. Meanwhile, $CoS_{1.97}$-CeO_2 has a smaller Tafel slope of 49 mV dec^{-1} through enhanced adsorption of OH^-, fast electron transfer and *in situ* formation of Co(IV)O_2 species under the OER condition. Furthermore, *operando* spectroscopic characterizations combined with theoretical calculations demonstrate that spatial architectures play a distinguished role in modulating the electronic structure and promoting the reconstruction from sulfide to oxyhydroxide towards higher chemical valence. The findings highlight spatial architectures and surface reconstruction in designing advanced electrocatalytic materials.

1. Introduction

Electrocatalytic water splitting is becoming a promising alternative for hydrogen production as sustainable green energy to solve the energy crisis and environmental problems.[1] However, the actual water splitting voltage is generally much higher than the theoretical value of 1.23 V, for the sluggish kinetics of hydrogen evolution reaction (HER) occurring at the cathode, and especially the oxygen evolution reaction (OER) with complex four-electron proton coupling process at the anode.[2] The current commercial Ir/Ru-based OER catalysts face the bottleneck of scale-up industrial application due to their scarce crustal distribution and exorbitant price.[3] Hence, there have been a great number of researches on non-precious metals materials with attractive OER performance, such as spinel oxides,[4] perovskites,[5] layered double hydroxides (LDHs) [6], *etc* benefit from the adjustable transition metal (TM) active sites with various strategy.[7] Cobalt sulfide with various structures are prospective substitutes for noble-metal catalysts as pre-catalysts derived from their intrinsic high conductivity and abundant redox chemistry.[8] For example, oxygen vacancies dominated NiS_2/CoS_2–O interface porous nanowires through *in situ* electrochemical oxidation of NiS_2/CoS_2 exhibits prominently better

OER performance with an overpotential of 235 mV at 10 mA cm^{-2}.[9] Besides, Hao et al.[10] reported a N-enriched CoS_2 catalyst through ammonium hydroxide-assisted N anion doping strategy, which exhibits 40 h stability under alkaline medium with a low overpotential. In addition, Qiu et al.[11] enhanced the OER activity of Co_9S_8 via P doping, which induces the optimized electronic structure and dual active sites effect. Briefly speaking, developing new Cobalt sulfide materials for OER is full of challenges and chances.[12]

Ceria (CeO_2) presents unique physicochemical properties such as excellent oxygen ion conductivity and oxygen storage capacity, which derive from the reversible variation between $Ce^{3+}$and Ce^{4+}, making a good candidate in both electrocatalysis and thermal catalysis as co-catalysts or support materials to improve activity and stability.[13] Recently, doping Ce atoms into CoS_2 dramatically weakens the surface O_2 adsorption and alleviates the leak of active components, bringing robust HER activity for more than 250 h.[14] Feng et al.[15] developed a novel FeOOH/CeO_2 heterolayer nanotubes (HLNTs) with CeO_2 layer coated grown on Ni foam. Benefit from the oxygen storage capacity of the outer CeO_2 layer and the strong electron interaction between two phases, the hybrid material has enhanced intermediate adsorption, thus better catalytic activity. In addition, ceria is also used as an oxygen-vacancies-rich substrate to regulate the electronic structure of supported materials. Long et al.[16] synthesized nickel-decorated transition metal oxide nanosheets on ceria film (ceria/Ni-TMO), displaying the overpotential of 220 mV at 10 mA cm^{-2} due to abundant active centers and the synergistic effect of Ni-TMO and CeO_2 film. It is worthy that Xia et al.[17] confirmed that the high-speed electron transfer between nickel–iron–chromium hydroxide (NFC) and underlying CeO_2 could be established through 3d−4f electronic ladders induced by the interfacial interaction, demonstrating a feasible strategy to assemble TM-based electrocatalysts with CeO_2 material. Furthermore, Gao et al.[18] originally discovered that NiO with CeO_2 clusters embedded shows better OER performance than the CeO_2-surface-loaded attribute to more active sites and the

activation of adsorbed water on unsaturated Ce sites via intimate contact. Though numerous researches have provided comprehensive discussions on the promotion of ceria for OER activity, these works are mainly based on only one kind of spatial configuration (supporting or inverse loading). Efforts on the rational design and manipulation of advanced ceria-incorporated hybrid materials via spatial architectures engineering have not been systemically investigated.[19] Deep insight into the effect between specific spatial architectures and catalytic properties is attractive but challenging, which could play a critical role in guiding the design and synthesis of high performance electrocatalysts.

Here, we report a novel strategy of two $CeO_2/CoS_{1.97}$ heterostructure with different spatial architectures and investigate their electronic structures, reconstruction behaviors and OER performances to comprehensively understand the structure-performance relationships. The CeO_2 layer plays distinct roles depending on configurations for OER performances. To be specific, the CeO_2 substrate supported $CoS_{1.97}$ (CeO_2-$CoS_{1.97}$) delivers a lower potential of reconstruction transition, smaller overpotential of 264 mV at 10 mA cm^{-1} and long-term durability, which benefits from the abundant active sites derived from lattice disorder. Whereas $CoS_{1.97}$ with CeO_2 surface decorated ($CoS_{1.97}$-CeO_2) exhibits easier transformation into CoOOH active phase along with CoO_2 species and smaller Tafel slope of 49 mV dec^{-1}, which only requires the overpotential of 323 mV to reach 100 mA cm^{-1}, indicating its favorable OER kinetics under large current.

2. Results and Discussion

2.1. Structure and Morphology

As illustrated in **Figure S1**, $CeO_2/CoS_{1.97}$ heterostructures with different CeO_2 layer spatial architectures were prepared by alternating the relative order of electrodeposition and

hydrothermal procedure on carbon fiber paper (CFP), and then went through the same sulfidation process. The X-ray diffraction (XRD) patterns in **Figure 1a** are assigned to the pyrite phase of $CoS_{1.97}$ (JCPDS no. 83-0573, space group Pa-3), which is widely acknowledged as ideal electrocatalysts due to its fully octahedral coordinated metal sites.[20] It is notable that the introduction of ceria effectively suppresses the oxidation of $CoS_{1.97}$, as confirmed by the disappearance of diffraction peaks at 31° indexed to (220) plane of Co_3O_4 phase compare to the $CoS_{1.97}$ sample. There is no discernible diffraction peak for CeO_2, which might result from the low concentration of Ce (2.14% for CeO_2-$CoS_{1.97}$, 3.76% for $CoS_{1.97}$-CeO_2 in atom ratio obtained from inductively-coupled plasma atomic emission spectrometry (ICP-AES)) and the similar lattice parameters of CeO_2 as $CoS_{1.97}$. The individual CeO_2 shows an XRD pattern indexed to the cubic structure of ceria (JCPDS no. 75-0076, space group Fm-3m) with a rough surface composed of ultrafine nanoparticles (**Figure S2**). As shown in field emission scanning electron microscope (FE-SEM) images (**Figure 1b−d**), the freestanding materials feature similar array clusters morphology interlaced with nanoplates vertically grown on CFP. To investigate the elemental distribution of each spatial configuration, SEM energy dispersive spectrum (EDS) mappings were conducted. The Ce and O elements of CeO_2-$CoS_{1.97}$ concentrate in the region near CFP (**Figure S3**) but uniformly distribute with Co and S for $CoS_{1.97}$-CeO_2 (**Figure S4**), confirming the successful preparation of two hybrid materials with distinct spatial architectures. In detail, as shown in transmission electron microscopy (TEM) images (**Figure S5**), the nanoplate is assembled with sub-unit nanoparticles, and the ceria-incorporation preserves the nanoplates morphology meanwhile interconnected bi-continuous porous structures are formed, which could facilitate mass transfer in electrocatalysis.[21] The corresponding TEM mappings depict the uniform distribution of elements for hybrid materials in one nanoplate, indicating the strong coupling of ceria and sulfide at the nanoscale (**Figure S6**). **Figure 1e−g** display the HR-TEM images of series materials, where the hybrids with

different spatial architectures exhibit distinct atom arrangements around heterointerface perimeters. **Figure 1e** presents the lattice fringes with the spacing of 0.223 nm, which is assigned to (211) of $CoS_{1.97}$. The clear and continuous lattice fringes in **Figure 1h** also confirm the good crystallinity of pure phase material. As for CeO_2-$CoS_{1.97}$ in **Figure 1f**, the lattice spacing of 0.195 and 0.305 nm are assigned to the (220) and (111) of $CoS_{1.97}$ and CeO_2, respectively. Despite there is a "sharp" heterointerface between the two components, their fringes coherently contact with each other within interface-perimeter without obvious lattice distortion (**Figure 1i**). The unique spatial configuration induces the hetero-mutual interaction and the compressive stress of upper sulfide at the same time for the CeO_2 in the interlayer with the obviously shrink of lattice spacing of (111). However, $CoS_{1.97}$-CeO_2 shows a gradual change of "mosaic-like" harmonious coupled atom arrangements across the edge of adjacent domains rather than defect-rich amorphous grain boundary (**Figure 1j**), where fringes with lattice spacings of 0.275 and 0.191 nm are indexed to (200) of $CoS_{1.97}$ and (220) of CeO_2, respectively (Figure 1g). Thus, there is diverse intimate atomic coupling between ceria and sulfide in each hybrid catalyst relying on the specific configurations, confirming the formation of nanohybrids and the existence of strong interaction between two phases.

Electrocatalysis is a surface/interface process at electrode/electrolyte, therefore hydrophilicity is of vital importance. Wettability measurements display that the contact angle of as-prepared $CoS_{1.97}$ is 85°, while CeO_2 substrate, CeO_2-$CoS_{1.97}$ and $CoS_{1.97}$-CeO_2 all display superhydrophilic properties with the contact angle of 0° (**Figure 1k**). The heterointerfaces endow hybrids with better superhydrophilic properties as demonstrated by the droplet spreading time, concretely 0.81 s, 1.80 s and 2.74 s for $CoS_{1.97}$-CeO_2, CeO_2-$CoS_{1.97}$, CeO_2, respectively. Further as clarified in electron spin resonance (ESR) spectra (**Figure S7**), $CoS_{1.97}$ shows a weaker signal, while $CoS_{1.97}$-CeO_2 has a stronger signal of oxygen vacancies than CeO_2-$CoS_{1.97}$ and CeO_2. In brief, the improvement of hydrophilicity is attributed to the oxygen vacancies of

ceria, and $CoS_{1.97}$-CeO_2 shows the best wettability resulted from more exposure of ceria medicated surface sites.

2.2 Electronic Structure

To deeply investigate the electronic structure and coordination environment of the materials, X-ray photoelectron spectroscopy (XPS) and X-ray absorption fine structure (XAFS) were carried out. **Figure 2a** shows the XPS spectra of Co 2p, the main peaks at 779.0 eV and 780.7 eV are attributed to Co^{3+} $2p_{3/2}$ and Co^{2+} $2p_{3/2}$, respectively, demonstrating the coexistence of Co^{3+} and Co^{2+} in $CoS_{1.97}$ sample. The binding energy of Co^{2+} $2p_{1/2}$ exhibit 0.2 eV positive shift in CeO_2-$CoS_{1.97}$ and 0.4 eV negative shift in $CoS_{1.97}$-CeO_2 compared to $CoS_{1.97}$, while the ratio of Co^{2+}/Co^{3+} change from 1.05 to 1.44 and 0.97 for CeO_2-$CoS_{1.97}$ and $CoS_{1.97}$-CeO_2, respectively, revealing the strong electron interaction between CeO_2 and $CoS_{1.97}$. In Ce 3d spectra, the peak of v, v_2, v_3 and u, u_2, u_3 correspond to Ce^{4+} $3d_{5/2}$ and $3d_{3/2}$, whereas the v_1 and u_1 correspond to Ce^{3+} $3d_{5/2}$ and $3d_{3/2}$, respectively (**Figure 2b**).[22] The ratio of Ce^{3+} significantly increases in hybrids than CeO_2, especially for CeO_2-$CoS_{1.97}$, suggesting the higher concentration of oxygen vacancies to balance charge distribution in heterostructures. The O 1s spectra could be divided into O1 at about 529.4 eV for lattice O^{2-}, O2 at 531.3-531.8 eV for vacancies oxygen or OH^- groups, 532.8-533.4 eV for adsorbed water or S−O species (**Figure 2c**).[23] $CoS_{1.97}$-CeO_2 has the highest O2 ratio (67.91%) than CeO_2-$CoS_{1.97}$ (65.38%) and CeO_2 (50.91%). In S 2p spectra from **Figure 2d**, the dominant double peaks locate at 162-165 eV correspond to Co−S bonds, and the broad peak at 168 to 171 eV is assigned to the S−O bonds caused by surface oxidation when exposed to air atmosphere. Furthermore, the increase of Co−S bonds in both Co 2p and S 2p after ceria incorporated is from the strong coupling between the CeO_2 and $CoS_{1.97}$, which coincides with the HR-TEM. Thus, the strong electron interactions

between Co^{2+}/Co^{3+} and $Ce^{3+}-O_v$ sites are established on the strong interaction between ceria and sulfides across the heterointerfaces.

As shown in Co K-edge X-ray absorption near edge spectroscopy (XANES) from **Figure 2e**, the sulfide samples exhibit a relatively broader absorption edge compared to the oxide standard samples.[24] CeO_2-$CoS_{1.97}$ has a similar absorption edge energy compared to $CoS_{1.97}$ counterpart but a remarkably lower intensity of the white line peak, indicating its higher degree of lattice disorder and less unoccupied electronic states.[25] While for $CoS_{1.97}$-CeO_2, the absorption edge dramatically shifts to higher energy in coincidence with XPS in Figure 2a, demonstrating the relatively low electron density of Co sites, which is favorable to nucleophilic attack by OH^-. Extended X-ray absorption fine structure (EXAFS) of Co K-edge was conducted to reveal the local chemical environment of Co sites. As shown from Fourier transform (FT) in *R* space (**Figure 2f**), series sulfides show obviously different coordination environments from oxides. CeO_2-$CoS_{1.97}$ has a similar single scattering path as $CoS_{1.97}$, but slightly longer in first shell coordination of Co−S paths (1.78 Å) than $CoS_{1.97}$ (1.75 Å) caused by lattice disorder with oxygen-defects-rich ceria supported.[26] For $CoS_{1.97}$-CeO_2, the peak negatively shifts to 1.60 Å, indicating its shorter first shell coordination distance. As illustrated in Continuous Cauchy wavelet transform (CCWT) (**Figure 2g**), the intensity maximum near 3.41 Å of CeO_2-$CoS_{1.97}$ is similar to $CoS_{1.97}$, suggesting the same Co−Co contributions. However, the main intensity maximum of $CoS_{1.97}$-CeO_2 occurs between $CoS_{1.97}$ and CoO in both *R* and *k* space, while the intensity maximum at 4.56 Å assigned to Co−Co contribution is the same as that in CoO. In combination with the XANES, $CoS_{1.97}$-CeO_2 exhibits the coordination structure of Co sites as a mixture of CoO and $CoS_{1.97}$, which is aroused by the $Co^{3+}-O_v-Ce^{3+}$ electron interaction between CeO_2 and $CoS_{1.97}$.[27] Furthermore, the chemical structure of CoO is kinetically facile to transform into oxyhydroxide active phase in alkaline medium and reacts as active skin to drive subsequent reconstruction of the inner part.[28]

2.3 Pre-oxidation Process and OER Performance

The heterostructures were then measured in an alkaline medium without iR-correction to evaluate their pre-oxidation behaviors. As the first cyclic voltammetry (CV) curve shown in **Figure 3a**, both hybrid materials exhibit earlier oxidation peaks of the Co^{2+}/Co^{3+} redox than $CoS_{1.97}$. The transition potential of CeO_2-$CoS_{1.97}$ is the lowest (1.12 V), followed by $CoS_{1.97}$-CeO_2 (1.14 V) and $CoS_{1.97}$ (1.21 V). At the same time, the steep current baselines, the characteristic of separated positive and the negative scanning curves at the OER region all indicate that the oxidation process of Co^{2+} is coupled with the oxidation corrosion of sulfur. During the 11 cycles of the CV process, CeO_2-$CoS_{1.97}$ and $CoS_{1.97}$-CeO_2 gradually reach stable states after 3 cycles, while the Co^{2+}/Co^{3+} oxidation peak of $CoS_{1.97}$ negative shifts to a lower potential and exhibit negligible changes during subsequent cycles after the first cycle (**Figure S8**). As for the steady final state (11th CV),). The potential difference between oxidation and reduction peaks is about 59 mV, further confirming that the redox current is from the one-electron-evolved Co^{2+}/Co^{3+} redox (**Figure 3b**). In the higher potential interval, the pair of redox species is ascribed to Co^{3+}/Co^{4+}, and it is overlapped with the onset of the OER process. The obviously negative shifts of cathodic peaks prove that the Co sites in hybrids are facile to be oxidized to high valence states, which are recognized as higher intrinsic activity sites.[29] Further, the double-layer capacitance (C_{dl}) tests show that CeO_2-$CoS_{1.97}$ has the largest value of C_{dl} (8.96 mF cm^{-2}) than $CoS_{1.97}$-CeO_2 (7.61 mF cm^{-2}) and $CoS_{1.97}$ (5.03 mF cm^{-2}), indicating that CeO_2-$CoS_{1.97}$ possesses more active sites result from the high degree of lattice disorder (**Figure 3c**, **Figure S9**). The introduction of oxygen-vacancies-rich ceria remarkably increases the electrochemical surface area (ECSA) of electrocatalysts, which is coincided with the incensement of the peak areas and pseudocapacitive current in CV cycles from Figure 3b. It is worth noting that the large ECSA of commercial Ir/C (12.57 mF cm^{-2}) comes from the size effect.

OER performances were then evaluated in 1 M KOH using linear sweep voltammetry (LSV) (for details please see Methods in Experimental Section). CeO_2-$CoS_{1.97}$ exhibits the lowest overpotential of 264 mV to reach a current density of 10 mA cm^{-2}, which is similar to $CoS_{1.97}$-CeO_2 (270 mV) and much lower than $CoS_{1.97}$ (310 mV) or Ir/C catalyst (290 mV) (**Figure 3d**). Furthermore, as for kinetics criterion, $CoS_{1.97}$-CeO_2 shows an extraordinarily small Tafel slope (49 mV dec^{-1}), smaller than CeO_2-$CoS_{1.97}$ (64 mV dec^{-1}), $CoS_{1.97}$ (69 mV dec^{-1}) and Ir/C (74 mV dec^{-1}) (**Figure 3e**). The CeO_2 displays ignorable catalytic activity with the overpotential of 554 mV at10 mA cm^{-2} and a tremendous Tafel slope of 442 mV dec^{-1} (**Figure S10**). The rapid kinetic endows $CoS_{1.97}$-CeO_2 with better large current performance, and it only requires 323 mV to reach 100 mA cm^{-2}, while CeO_2-$CoS_{1.97}$ only has 65 mA cm^{-2} at the same overpotential. The electrochemical impedance spectroscopy (EIS) also demonstrate that CeO_2-$CoS_{1.97}$ comes with slightly smaller charge transfer resistance (R_{ct}) of 1.09 Ω than $CoS_{1.97}$-CeO_2 (1.13 Ω), and both of their R_{ct} is much smaller than $CoS_{1.97}$ (2.64 Ω), indicating their more favorable charge transfer at electrode/electrolyte interfaces (**Figure S11**, **Table S1**). In view of the overpotential and Tafel slope, $CoS_{1.97}$-CeO_2 heterostructure electrocatalyst with the spatial architecture of ceria surface decorated is competitive to most recent-reported Co-based sulfides and other TM-based/ceria hybrid materials (**Figure 3f, Table S2**). To further elucidate the charge transfer kinetics during the potential-dependent evolution, *operando* EIS measurements were performed from open circuit potential (OCP) to 1.77 V. **Figure 3g** shows that Co^{2+} in $CoS_{1.97}$-CeO_2 is rapidly oxidized to Co^{3+} above 1.17 V, while the oxidation processing of Co^{3+} is relatively slower than that of Co^{2+}. The redox process of Co^{3+}/Co^{4+} is overlapped with the OER process within 1.27 to 1.57 V, which is precisely consistent with the trend of CV curves (**Table S5**). The CeO_2-$CoS_{1.97}$ and $CoS_{1.97}$ have similar electrochemical behaviors (**Figure S12**), except that $CoS_{1.97}$ shows obviously higher R_{ct} within the Co^{4+} formation process and the OER dominant region (above 1.57 V), inversely indicating the

favorable interfacial electron transfer and optimized OH^- adsorption kinetics of hybrid materials (**Figure 3h**, **Table S3-4**).

Long-term durability beyond high activity is necessary for practical application. As **Figure 3i** shown, heterostructures maintain the lower potential at 10 mA cm^{-2} for over 50 h without a noticeable rise of potential while $CoS_{1.97}$ exhibits an observable decay within 24 hours. To shed light on both activity and stability, characterizations of morphology, crystal and electronic structure were carried out after the stability tests. In SEM images after durability tests (**Figure S13**), $CoS_{1.97}$ is almost stripped off from the conductive substrate by the strong impact of O_2 bubbles. Whereas, CeO_2-$CoS_{1.97}$ presents the interlaced nanoplates array morphology by assembled hexagonal nanosheets, which is facile to expose edge active sites and evolve O_2 bubbles in time. The stable CeO_2/$CoS_{1.97}$ interfaces effectively prohibit the underlying scaffold from damage under harsh conditions. Benefit from the oxygen storage capacity of surface CeO_2 layer which further serves as buffer nodes to release stress from drastic reconstruction, $CoS_{1.97}$-CeO_2 roughly preserves the initial morphology.[30] And the XRD patterns consistent with Raman spectra after OER in **Figure S14** illustrate the kinetic favorable amorphous Co-based (oxy)hydroxide under OER condition (Figure S13b), which also favors the penetration of electrolyte and exposure of active sites to promote the reconstruction of the active phase.[31] TEM images in **Figure S15a−c** further confirm the nanoplate morphology of $CoS_{1.97}$ and $CoS_{1.97}$-CeO_2, and the small nanosheets morphology of CeO_2-$CoS_{1.97}$ with SEM images. As shown in HR-TEM images after OER (**Figure S15d−f**), $CoS_{1.97}$ still retains clear lattice fringes, while CeO_2-$CoS_{1.97}$ coats a random amorphous layer on coarse $CoS_{1.97}$ nanoparticles. For $CoS_{1.97}$-CeO_2 samples, there are abundant ultrafine CoOOH nanoparticles densely dispersing in $CoS_{1.97}$ and CeO_2 matrices in the form of amorphous layer. To satisfy the large current demand of industrial water splitting, chronopotentiometry tests were performed at 1000 mA cm^{-2} using the hybrid materials directly grown on graphite plates. As shown in **Figure S16**,

two hybrid catalysts all remain lower potential at least 150 h and CeO_2-$CoS_{1.97}$ exhibits relatively steady performance, while the voltage required for $CoS_{1.97}$ sharply raises after 60 hours.

2.4 Surface Reconstruction

To unveiling the mechanism of surface reconstruction, XPS spectra after durability were collected. The binding energy of Co 2p in all samples shift positively due to the transformation from sulfide to oxyhydroxide along with the disappearance of M−S bonds and increment of S−O bonds in S 2p (**Figure 4a−b**). The S−S bonds in pyrite are oxidized to SO_4^{2-} with a small amount still remained in the lattice near Co sites, which further enhances the OER activity.[32] Furthermore, the ratio of v_1 and u_1 peak for Ce^{3+} significantly reduce after the stability test, indicating that Ce^{3+}−O_v sites also have participated in the reconstruction process (**Figure S17**). The positive shift of M−O bonds for CeO_2-$CoS_{1.97}$ and negative shift for $CoS_{1.97}$-CeO_2 compared with $CoS_{1.97}$ result from the interaction between Ce−O bonds and Co−O bonds (**Figure 4c**), which confirm the moderation of electronic structure for as-restructured materials in different spatial architectures. The main peaks at 531.3 eV are ascribed to Co−OH bonds, which further confirm the generation of CoOOH phase after OER. It is obvious that post-characterizations of materials for OER are insufficient to accurately reproduce their real reconstruction transformation and monitor the authentic active intermediate.

Hence, *in situ* Raman spectra were performed to track the transformation during electrochemical reconstruction. The peak at 286 cm^{-1} and 389 cm^{-1} are ascribed to the typical E_g and A_g vibrational modes of pyrite $CoS_{1.97}$. (**Figure 4d**). The half width of A_g peak in CeO_2-$CoS_{1.97}$ and $CoS_{1.97}$-CeO_2 has broadened 50% and 30% compared with $CoS_{1.97}$, respectively, suggesting the smaller domain sizes and a higher degree of lattice disorder (**Figure 4e−f**). With the increase of applied potential, the peak at 500 cm^{-1} and broad peak stretching over 550-650

cm^{-1} are assigned to E_g and A_g vibrational modes of CoOOH,[33] respectively, which gradually get weaker of peaks indexed to sulfides. Specifically, the A_g peaks of CeO_2-$CoS_{1.97}$ and $CoS_{1.97}$-CeO_2 appear to weaken at a lower potential than $CoS_{1.97}$, while CeO_2-$CoS_{1.97}$ exhibits a more widened E_g peak and $CoS_{1.97}$-CeO_2 shows the higher intensity of E_g peak, suggesting the higher defect concentration and transformation degree of CoOOH in CeO_2-$CoS_{1.97}$ and $CoS_{1.97}$-CeO_2 respectively. Notably, as shown in Figure 4f for $CoS_{1.97}$-CeO_2, the intensity of peaks ascribed to CoOOH become abnormally strong, while the E_g and A_g peaks gradually red shift to 479 cm^{-1} and 583 cm^{-1}, respectively, above 1.50 V, suggesting the generation of abundant CoO_2 phase with higher valence state.[34] The similar peak shift is hard to distinguish in $CoS_{1.97}$ and CeO_2-$CoS_{1.97}$, beacuse the generation of Co(IV) species might be too limited to detect by *in situ* Raman spectra. As for $CoS_{1.97}$-CeO_2, the accelerated adsorption and dissociation of H_2O facilitated by the Ce^{3+}−O_v sites promote easier transition of CoOOH, which endows $CoS_{1.97}$-CeO_2 with optimized OER kinetics.

The *quasi-operando* XPS spectra was also carried out to complementally understand the role of ceria-incorporation in reconstruction process. As depicted in **Figure 4g−i**, once the sulfides immerse into alkaline electrolyte, the peaks of Co−O bonds at 781.3 eV appear, which is significantly different from the Co−S bonds at 778.9 eV. The similar pre-oxidation behaviors are also identified in situ Raman spectra (**Figure S18**), with the appearance of Eg peaks of CoOOH at 500 cm^{-1} after full contact with electrolyte. The peaks of M−O bonds emerge in O 1s spectra due to the oxygen exchange between the active sites and electrolyte (**Figure S19a−c**). When applied potential increases, the signals of the Co−S bonds become weaker while the Co−O bonds gradually shift to lower binding energy and eventually locating at 780.3 eV. Meanwhile, the M−O bonds in O 1s negatively shift and eventually stabilize at 529.5 eV, indicating the formation of CoOOH species before OER (**Figure S19a−c**). Unusually, the intensity of Co−O bonds for $CoS_{1.97}$-CeO_2 at OCP is evidently higher than the others,

suggesting the spontaneous oxygen exchange and faster reconstruction benefit from the stronger absorption of OH^- and higher oxygen ion conductivity at the surface (Figure 4i).[35] The potential-dependent phase-transition behavior is further confirmed by the decay of Co−S bonds in S 2p spectra from 0.97 V to 1.27 V (**Figure S19d−f**). However, there are still considerable amounts of remained SO_4^{2-} species above 1.27 V, which also contribute to the OER performances. From Figure 4g−i, the complete transition potential of CoOOH for $CoS_{1.97}$, CeO_2-$CoS_{1.97}$, $CoS_{1.97}$-CeO_2 are 1.37, 1.17 and 1.27 V, respectively, the same trend as CV curves and Raman spectra. Clearly, $CoS_{1.97}$ with the defect-rich CeO_2 layer supported has a higher degree of lattice disorder, more Co^{2+} active sites, and extended Co−S bonds, which could remarkedly reduce the transition energy barrier of CoOOH. However, the surface decorated CeO_2 layer serves as oxygen buffer and functional junction to enhance the wettability, oxygen exchange capacity and electron transfer of Co^{3+}–O_v–Ce^{3+} active skin, which promotes the generation of more ultrafine CoOOH and CoO_2 species.

2.5 Density Functional Calculations

Furthermore, we have carried out the theoretical calculations to investigate the origins of distinct OER performances of CeO_2-$CoS_{1.97}$ and $CoS_{1.97}$-CeO_2 induced by the spatial architectures. The composite structure has been constructed based on the experimental characterizations. For CeO_2-$CoS_{1.97}$, the electroactive region is dominated by the surface. The interface structure displays high stability with limited structural distortion, which guarantees the durability of the electrocatalysts. The high electroactivity of the surface facilitates the electron transfer from the CeO_2-$CoS_{1.97}$ to the adsorbates (**Figure 5a**). In comparison, the $CoS_{1.97}$-CeO_2 demonstrates distinct electronic structures. It is noted that the interfacial region has demonstrated the electron-rich feature due to the strong interactions with CeO_2, which supports the good electron transfer for the OER. The surface oxygen vacancy sites of CeO_2 are

electroactive, which facilitate the adsorption of *OH in the alkaline media. The introduction of CeO_2 on the surface can further suppress the oxidation of the $CoS_{1.97}$ and Co leaching during the OER (**Figure 5b**). Then, we compare the electronic structure of these two catalysts by the projected partial density of states (PDOS). We notice that both $CoS_{1.97}$-CeO_2 and CeO_2-$CoS_{1.97}$ have shown a similar electronic structure, which is consistent with their close OER performance. In CeO_2-$CoS_{1.97}$, the dominant peak of Co-3d orbital locates at E_V-1.35 eV (E_V denotes 0 eV), which is slightly lower than that in $CoS_{1.97}$-CeO_2, supporting the higher concentration of Co^{2+}. More evidently, the O-s,p orbitals have obviously become more electron-rich more electron-rich. In comparison, the Ce-4f and 5d show the relatively stable electronic structure as the XPS results (**Figure 5c**). In $CoS_{1.97}$-CeO_2, we notice the evident peak Co-3d close to the Fermi level (E_F), occupying the position of E_V-1.29 eV (E_V denotes 0 eV), indicating the higher concentration of Co^{3+}. The s,p orbitals of S sites cover a broad range and even cross the E_F, supporting the good conductivity. Meanwhile, the s,p orbitals of O sites locate below the Co-3d orbitals from E_V-0.60 eV to E_V-4.90 eV. The Ce-4f orbitals show a good overlap with the Co-3d orbitals to promote the electron transfer at the interface (**Figure 5d**). Although the formation of CoOOH is noted in both heterostructures, the varied electronic structures of CeO_2/$CoS_{1.97}$ and $CoS_{1.97}$/CeO_2 also determine the different potentials of forming CoOOH species. In CeO_2-$CoS_{1.97}$, we notice a slight downshifting trend of the Co-3d orbitals, which indicates the increasing concentration of Co^{2+} on the surface, which supports easier oxidation to form the CoOOH for promoting the OER performances. These results are supportive of the experimental characterizations (**Figure 5e**). In comparison, for $CoS_{1.97}$-CeO_2, the Co-3d orbitals all demonstrate a higher position than the Co-3d in the pristine $CoS_{1.97}$. From bulk to the interface with CeO_2, the Co-3d orbitals have upshifted from E_V-1.93 eV to E_V-0.80 eV, indicating the increasing valence states of Co sites at the interface. However, due to the protection coverage of CeO_2 on the surface, the applied potential to form CoOOH in

$CoS_{1.97}/CeO_2$ will be slightly increased, supporting the experimental results (**Figure 5f**). Then, we further notice the nearly linear correlation to the σ orbitals of the key intermediates during OER, from the initial adsorption of OH* towards the final desorption of formed O_2. The different material structures lead to the varied peak position of σ orbitals, the linear correlation determines the electron transfer efficiency. Notably, for both $CoS_{1.97}$-CeO_2 and CeO_2-$CoS_{1.97}$, the σ orbitals of *OOH deviate from the linear correlation, which demonstrates that the transformation from O* to *OOH is the potential rate-determining step (RDS) of OER (**Figure 5g−h**).

The energetic reaction pathway and the overpotential have been displayed. For both structures, we notice the largest energy barriers occur at the conversion from [$O^*+H_2O+2OH^-+2e^-$] to [$OOH^*+H_2O+OH^-+e^-$] with an energy barrier of 1.46 and 1.47 eV, respectively. In addition, the CeO_2-$CoS_{1.97}$ shows a slightly stronger desorption capability than $CoS_{1.97}$-CeO_2 due to the smaller energy barrier at the final step of OER (**Figure 5i**). The overpotentials have been estimated under the potential of 1.23 V. We notice that $CoS_{1.97}$-CeO_2 demonstrates a stronger *OH adsorption, which is distinct from the spontaneous conversion from *OH to O* in CeO_2-$CoS_{1.97}$. Both the structures show no barriers for the last reaction of [O_2+2H_2O], which supports the high performance of OER. Meanwhile, from the binding energies of O_2, CeO_2-$CoS_{1.97}$ supports a faster mass transport. The calculated overpotential are 0.24 and 0.23 eV for $CoS_{1.97}$-CeO_2 and CeO_2-$CoS_{1.97}$, respectively (**Figure 5j**). Although CeO_2-$CoS_{1.97}$ and $CoS_{1.97}$-CeO_2 have shown similar performance at 10 mA cm^{-2}, the origins are not the same due to different structure modulations via specific spatial architecture.

3. Conclusion

In summary, we construct two freestanding $CeO_2/CoS_{1.97}$ heterostructures with different spatial architectures (CeO_2-$CoS_{1.97}$ with CeO_2 layer supported and $CoS_{1.97}$-CeO_2 with CeO_2 surface decorated) to boost OER performances. The introduction of CeO_2 into $CoS_{1.97}$ leads to distinct optimized electronic structures and plays a vital role in promoting OER activity due to the diverse heterostructure pattern. Concretely, the oxygen-vacancies-rich CeO_2 substrate enables CeO_2-$CoS_{1.97}$ to expose more active sites and lower transition potential of CoOOH, thus achieving a current density of 10 mA cm^{-2} at an overpotential of 264 mV as well as stable OER with over 150 h long-term stability in the alkaline medium. In comparison, $CoS_{1.97}$-CeO_2 shows the advantages of stronger adsorption of OH^- and coordination structure to promote the reconstruction of surface Co-species into CoOOH even Co(IV) species along with high conductivity and fast electron transfer across heterointerface, which endows $CoS_{1.97}$-CeO_2 favorable catalytic kinetics with small Tafel slope of 49 mV dec^{-1} and η of 323 mV at 100 mA cm^{-2}. This work sheds light on designing and fabricating advanced heterostructure electrocatalysts via a ceria functional layer with specific spatial architectures to modulate the electronic structures, stabilize the interfacial perimeter as well as promote the reconstruction process, which all lead to enhanced electrocatalytic performances.

4. Experimental Section

Chemical Materials: Cobalt(II) nitrate hexahydrate ($Co(NO_3)_2 \cdot 6H_2O$, AR), sodium citrate ($C_6H_5Na_3O_7$, TSC, AR), urea (CH_4N_2O, AR), cerium(III) nitrate hexahydrate ($Ce(NO_3)_3 \cdot 6H_2O$, AR), sodium chloride (NaCl, AR), sulfur powder (AR), nitric acid (HNO_3, GR) and potassium hydroxide (KOH, AR), commercial iridium carbon catalyst (20 wt%), N,N-dimethylformamide (DMF) and Nafion® (5 wt%) were purchased from Aladdin. The commercial carbon fiber papers (CFP) were purchased from Fuel Cell Store. All the chemicals were used as received

without further purification. All the standard solutions were prepared with Milli-Q water with a resistance of 18.25 MΩ·cm.

Synthesis of $Co(CO_3)_{0.5}(OH)\cdot 0.11H_2O$ (CoCH): The CoCH on CFP was synthesized by hydrothermal method. Prior to synthesis, CFP (3 cm × 4 cm) was hydrophilic pretreatment with HNO_3 and ethanol, rinsed by deionized (DI) water, and then ultrasonicated in ethanol and water alternately for several times. A piece of CFP was immersed and ultrasonicated in the 70 mL aqueous solution containing 2.0335 g $Co(NO_3)_2\cdot 6H_2O$, 2.1000 g urea, and 0.0257 g TSC for 10 min. Then, the solution was transferred into a 100 mL Teflon-lined stainless-steel autoclave and maintained at 95 °C for 8 hours. The as-synthesized electrode was rinsed with water several times, dried at 60 °C for 8 hours to get the CoCH.

Synthesis of CeO_2 Substrate: The CeO_2 layers on CFP were prepared according to previous literature report.[15] Typically, The CeO_2 film was *in situ* coated on the surface of CFP (2 cm × 3 cm) by electrodeposition in solution of 2 mM $Ce(NO_3)_3$ and 10 mM NaCl at 0.25 mA cm^{-2} for 10 min at 70 °C. Then the as-synthesized electrode was rinsed with ethanol for several times, dried at 60 °C.

Synthesis of CeO_2-$CoS_{1.97}$: First, the CeO_2-CoCH was prepared by hydrothermal method as the synthesis of CoCH except using the as-synthesized CeO_2 to replace the CFP as the substrate. Then, a piece of the as-obtained CeO_2-CoCH (2×3 cm) was placed in a porcelain boat together with 200 mg sulfur powder and the porcelain boat was heated at 450 °C for 2 hours in Ar atmosphere, and then naturally cooled to ambient temperature under the protection of Ar.

Synthesis of $CoS_{1.97}$-CeO_2: First, CeO_2 layer was deposited onto CoCH by *in situ* electrodeposition using the as obtained CoCH to replace CFP as substrate to get CoCH-CeO_2. Then $CoS_{1.97}$-CeO_2 was prepared by the sulfurization method mentioned above.

Physicochemical Characterizations: X-ray diffraction (XRD) measurements were carried out on Rigaku MiniFlex 600 diffractometer with Cu Kα radiation (λ=0.1542 nm) from 10° to 80° under a constant voltage of 40 kV. The morphology and EDX mapping of samples were analyzed by ThermoFisher Apreo S filed-emission scanning electron microscopy (FESEM) at an acceleration voltage of 30 kV. The contact angle measurements were carried out on a Kruss DSA100 optical contact angle/surface tension meter. Transmission electron microscopy (TEM) and high-resolution transmission electron microscopy (HR-TEM) pictures were obtained on a Tecnai G2 F30 filed emission transmission electron microscopy. Electron spin resonance (ESR) measurements were performed on a JES-FA300 electron spin resonance spectrometer at room temperature. X-ray photoelectron spectroscopy (XPS) analysis was made with a Kratos Axis Supra device and the data obtained was corrected with C 1s line at 284.8 eV. Inductively coupled plasma optical emission spectrometry (ICP-OES) analyses were performed on a Plasma Quant PQ9000 ICP spectrometer. Synchrotron radiation X-ray absorption fine structure (XAFS) spectroscopy at the Co K-edge were acquired in transmission mode using a Si (111) double-crystal monochromator at the 1W1B station of the Beijing Synchrotron Radiation Facility (BSRF). Raman spectroscopy measurements were conducted on a LabRAM HR Evolution spectrophotometer with 532 nm wavenumber of the excitation light source.

Electrochemical measurements: Electrochemical experiments were performed in fresh KOH on a CHI-760E Electrochemical Workstation (CHI Instruments) typical using a standard three-electrode system, while the large current stability tests were conducted in a four-electrode setup. Before the electrochemical measurement, the electrolyte was degassed by bubbling oxygen for at least 30 min to achieve a saturation condition of oxygen gas. All electrochemical investigations were performed at room temperature using a Hg/HgO as reference electrode, a Pt plate as counter electrode, and the test catalysts grown on the CFP substrates served as a working electrode in 1 M KOH unless otherwise specified. For Ir/C catalyst, homogeneous ink

was prepared by dispersing 2 mg commercial Ir/C (20 wt%) into 250 μL DMF, 700 uL ethanol and 50 μL Nafion solution (5 wt%). Next, 1000 uL ink was coated on CFP with an area of 2 cm^2 for catalytic tests. The measured potentials vs. reference electrode were converted to a reversible hydrogen electrode (RHE) according to the Nernst equation ($E_{RHE} = E_{Hg/HgO} + 0.0591 \times pH + 0.098$ and $E_{RHE} = E_{Ag/AgCl} + 0.0591 \times pH + 0.197$). Cyclic voltammetry (CV) measurements set 5 mV s^{-1} for peroxidation tests and 5 mV s^{-1} for averaging the positive-going and negative-going scan to obtain linear sweep voltammetry (LSV) plots.[36] *In situ* Raman spectra were investigated using a customized cell, with a saturated Ag/AgCl reference electrode and a Pt ring counter electrode in 0.1 M KOH. And the electrochemical impedance spectroscopy (EIS) tests were performed at different applied potentials vs. RHE in the frequency range of 0.01-100k Hz in 0.1 M KOH. Before *in situ* Raman, *operando* EIS and *quasi- operando* XPS tests, the CFP supported catalysts were carried out at applied potential for 10 min to obtain the surface chemical composition and structural information of materials.[37]

Calculation Setup: We applied the DFT calculations to investigate the electronic structure and energetic trend of CeO_2-$CoS_{1.97}$ and $CoS_{1.97}$-CeO_2 through the CASTEP packages.[38] The generalized gradient approximation (GGA) with Perdew-Burke-Ernzerhof (PBE) is chosen to describe the exchange-correlation energy.[39-41] We have set the cutoff energy of the plane-wave basis set to be the ultrafine quality of 380 eV based on the ultrasoft pseudopotentials. based on the Broyden-Fletcher-Goldfarb-Shannon (BFGS) algorithm, the k-points used in this work are applied with the coarse quality for the energy minimization.[42] For all the models, a 20 Å vacuum space has been set in the z-axis to guarantee full relaxation. To accomplish the geometry optimizations, the convergence test requires the Hellmann-Feynman forces should not exceed 0.001 eV/Å, the total energy difference should be less than 5×10^{-5} eV/atom and the inter-ionic displacement should be less than 0.005 Å, respectively.

Supporting Information

Supporting Information is available from the Wiley Online Library or from the author.

Acknowledgements

T.Y. D. and X. Z. contributed equally to this work. We acknowledge support from the National Natural Science Foundation of China (NO. 21931001 and 21922105). Special Fund Project of Guiding Scientific and Technological Innovation Development of Gansu Province (2019ZX-04) and the 111 Project (B20027). Bolong Huang acknowledges the support of the Natural Science Foundation of China (NSFC) (No. 21771156), and the Early Career Scheme (ECS) fund (Grant No. PolyU 253026/16P) from the Research Grant Council (RGC) in Hong Kong.

Received: ((will be filled in by the editorial staff))
Revised: ((will be filled in by the editorial staff))
Published online: ((will be filled in by the editorial staff))

References

[1] a) M. S. Dresselhaus, I. L. Thomas, *Nature* **2001**, *414*, 332; b) Y. Xue, L. Hui, H. Yu, Y. Liu, Y. Fang, B. Huang, Y. Zhao, Z. Li, Y. Li, *Nat. Commun.* **2019**, *10*, 2281; c) Z. W. Seh, J. Kibsgaard, C. F. Dickens, I. Chorkendorff, J. K. Nørskov, T. F. Jaramillo, *Science* **2017**, *355*, 4998.

[2] D. Yan, Y. Li, J. Huo, R. Chen, L. Dai, S. Wang, *Adv. Mater.* **2017**, *29*, 1606459.

[3] G. Wu, A. Santandreu, W. Kellogg, S. Gupta, O. Ogoke, H. Zhang, H.-L. Wang, L. Dai, *Nano Energy* **2016**, *29*, 83.

[4] a) J. Yin, J. Jin, M. Lu, B. Huang, H. Zhang, Y. Peng, P. Xi, C.-H. Yan, *J. Am. Chem. Soc.* **2020**, *142*, 18378; b) T. Wu, S. Sun, J. Song, S. Xi, Y. Du, B. Chen, W. A. Sasangka, H.

Liao, C. L. Gan, G. G. Scherer, L. Zeng, H. Wang, H. Li, A. Grimaud, Z. J. Xu, *Nat. Catal.* **2019**, *2*, 763.

[5] a) J. T. Mefford, X. Rong, A. M. Abakumov, W. G. Hardin, S. Dai, A. M. Kolpak, K. P. Johnston, K. J. Stevenson, *Nat. Commun.* **2016**, *7*, 11053; b) J. Hwang, R. R. Rao, L. Giordano, Y. Katayama, Y. Yu, Y. Shao-Horn, *Science* **2017**, *358*, 751.

[6] a) D. Zhou, Z. Cai, X. Lei, W. Tian, Y. Bi, Y. Jia, N. Han, T. Gao, Q. Zhang, Y. Kuang, J. Pan, X. Sun, X. Duan, *Adv. Energy Mater* **2018**, *8*, 1701905; b) R. Yang, L. An, Y. Zhang, N. Zhang, T. Dai, P. Xi, *ChemCatChem* **2019**, *11*, 6002.

[7] L. An, B. Huang, Y. Zhang, R. Wang, N. Zhang, T. Dai, P. Xi, C. H. Yan, *Angew. Chem. Int. Ed.* **2019**, *58*, 9459.

[8] M.-R. Gao, Y.-R. Zheng, J. Jiang, S.-H. Yu, *Acc. Chem. Res.* **2017**, *50*, 2194.

[9] J. Yin, Y. Li, F. Lv, M. Lu, K. Sun, W. Wang, L. Wang, F. Cheng, Y. Li, P. Xi, S. Guo, *Adv. Mater.* **2017**, *29*, 1704681.

[10] J. Hao, W. Yang, Z. Peng, C. Zhang, Z. Huang, W. Shi, *ACS Catal.* **2017**, *7*, 4214.

[11] B. Qiu, L. Cai, Y. Wang, X. Guo, S. Ma, Y. Zhu, Y. H. Tsang, Z. Zheng, R. Zheng, Y. Chai, *Small* **2019**, *15*, 1904507.

[12] a) R. Wang, Y. Wei, L. An, R. Yang, L. Guo, Z. Weng, P. Da, W. Chen, J. Jin, J. Li, P. Xi, *Chin. J. Chem.* **2020**, *38*, 772; b) D. Dong, Z. Wu, J. Wang, G. Fu, Y. Tang, *J. Mater. Chem. A* **2019**, *7*, 16068.

[13] J. Wang, X. Xiao, Y. Liu, K. Pan, H. Pang, S. Wei, *J. Mater. Chem. A* **2019**, *7*, 17675.

[14] J. Li, Z. Xia, M. Zhang, S. Zhang, J. Li, Y. Ma, Y. Qu, *J. Mater. Chem. A* **2019**, *7*, 17775.

[15] J.-X. Feng, S.-H. Ye, H. Xu, Y.-X. Tong, G.-R. Li, *Adv. Mater.* **2016**, *28*, 4698.

[16] X. Long, H. Lin, D. Zhou, Y. An, S. Yang, *ACS Energy Lett.* **2018**, *3*, 290.

[17] J. Xia, H. Zhao, B. Huang, L. Xu, M. Luo, J. Wang, F. Luo, Y. Du, C. H. Yan, *Adv. Funct. Mater.* **2020**, *30*, 1908367.

[18] W. Gao, Z. Xia, F. Cao, J. C. Ho, Z. Jiang, Y. Qu, *Adv. Funct. Mater.* **2018**, *28*, 1706056.

[19] W. Yang, X. Wang, S. Song, H. Zhang, *Chem* **2019**, *5*, 1743.

[20] S. Li, X. Hao, A. Abudula, G. Guan, *J. Mater. Chem. A* **2019**, *7*, 18674.

[21] H. Sun, C. Tian, G. Fan, J. Qi, Z. Liu, Z. Yan, F. Cheng, J. Chen, C. P. Li, M. Du, *Adv. Funct. Mater.* **2020**, *30*, 1910596 .

[22] X. He, X. Yi, F. Yin, B. Chen, G. Li, H. Yin, *J. Mater. Chem. A* **2019**, *7*, 6753.

[23] H. Xu, J. Cao, C. Shan, B. Wang, P. Xi, W. Liu, Y. Tang, *Angew. Chem. Int. Ed.* **2018**, *57*, 8654.

[24] N. Kornienko, J. Resasco, N. Becknell, C.-M. Jiang, Y.-S. Liu, K. Nie, X. Sun, J. Guo, S. R. Leone, P. Yang, *J. Am. Chem. Soc.* **2015**, *137*, 7448.

[25] Z. Li, A. Cao, Q. Zheng, Y. Fu, T. Wang, K. T. Arul, J. L. Chen, B. Yang, N. M. Adli, L. Lei, C. L. Dong, J. Xiao, G. Wu, Y. Hou, *Adv. Mater.* **2020**, *33*, 2005113.

[26] J. Hao, W. Luo, W. Yang, L. Li, W. Shi, *J. Mater. Chem. A* **2020**, *8*, 22694.

[27] A. Chen, X. Yu, Y. Zhou, S. Miao, Y. Li, S. Kuld, J. Sehested, J. Liu, T. Aoki, S. Hong, M. F. Camellone, S. Fabris, J. Ning, C. Jin, C. Yang, A. Nefedov, C. Wöll, Y. Wang, W. Shen, *Nat. Catal.* **2019**, *2*, 334.

[28] C.-W. Tung, Y.-Y. Hsu, Y.-P. Shen, Y. Zheng, T.-S. Chan, H.-S. Sheu, Y.-C. Cheng, H. M. Chen, *Nat. Commun.* **2015**, *6*, 8106.

[29] Y. Zhou, S. Sun, C. Wei, Y. Sun, P. Xi, Z. Feng, Z. J. Xu, *Adv. Mater.* **2019**, *31*, 1902509.

[30] M. S. Faber, R. Dziedzic, M. A. Lukowski, N. S. Kaiser, Q. Ding, S. Jin, *J. Am. Chem. Soc.* **2014**, *136*, 10053.

[31] S. Li, Z. Li, R. Ma, C. Gao, L. Liu, L. Hu, J. Zhu, T. Sun, Y. Tang, D. Liu, J. Wang, *Angew. Chem. Int. Ed.* **2021**, *60*, 3773.

[32] Y. Shi, W. Du, W. Zhou, C. Wang, S. Lu, S. Lu, B. Zhang, *Angew. Chem. Int. Ed.* **2020**, *59*, 22470.

[33] B. S. Yeo, A. T. Bell, *J. Am. Chem. Soc.* **2011**, *133*, 5587.

[34] A. Moysiadou, S. Lee, C.-S. Hsu, H. M. Chen, X. Hu, *J. Am. Chem. Soc.* **2020**, *142*, 11901.

[35] D. Cao, D. Liu, S. Chen, O. A. Moses, X. Chen, W. Xu, C. Wu, L. Zheng, S. Chu, H. Jiang, C. Wang, B. Ge, X. Wu, J. Zhang, L. Song, *Energy Environ. Sci.* **2021**, *14*, 906.

[36] C. Wei, R. R. Rao, J. Peng, B. Huang, I. E. L. Stephens, M. Risch, Z. J. Xu, Y. Shao-Horn, *Adv. Mater.* **2019**, *31*, 1806296.

[37] Z. Xiao, Y. C. Huang, C. L. Dong, C. Xie, Z. Liu, S. Du, W. Chen, D. Yan, L. Tao, Z. Shu, G. Zhang, H. Duan, Y. Wang, Y. Zou, R. Chen, S. Wang, *J. Am. Chem. Soc.* **2020**, *142*, 12087.

[38] S. J. Clark, M. D. Segall, C. J. Pickard, P. J. Hasnip, M. I. J. Probert, K. Refson, M. C. Payne, *Z. Kristall.* **2005**, *220*, 567.

[39] P. J. Hasnip, C. J. Pickard, *Comput. Phys. Commun.* **2006**, *174*, 24.

[40] J. P. Perdew, J. A. Chevary, S. H. Vosko, K. A. Jackson, M. R. Pederson, D. J. Singh, C. Fiolhais, *Phys. Rev. B* **1992**, *46*, 6671.

[41] J. P. Perdew, K. Burke, M. Ernzerhof, *Phys. Rev. Lett.* **1996**, *77*, 3865.

[42] J. D. Head, M. C. Zerner, *Chem. Phys. Lett.* **1985**, *122*, 264.

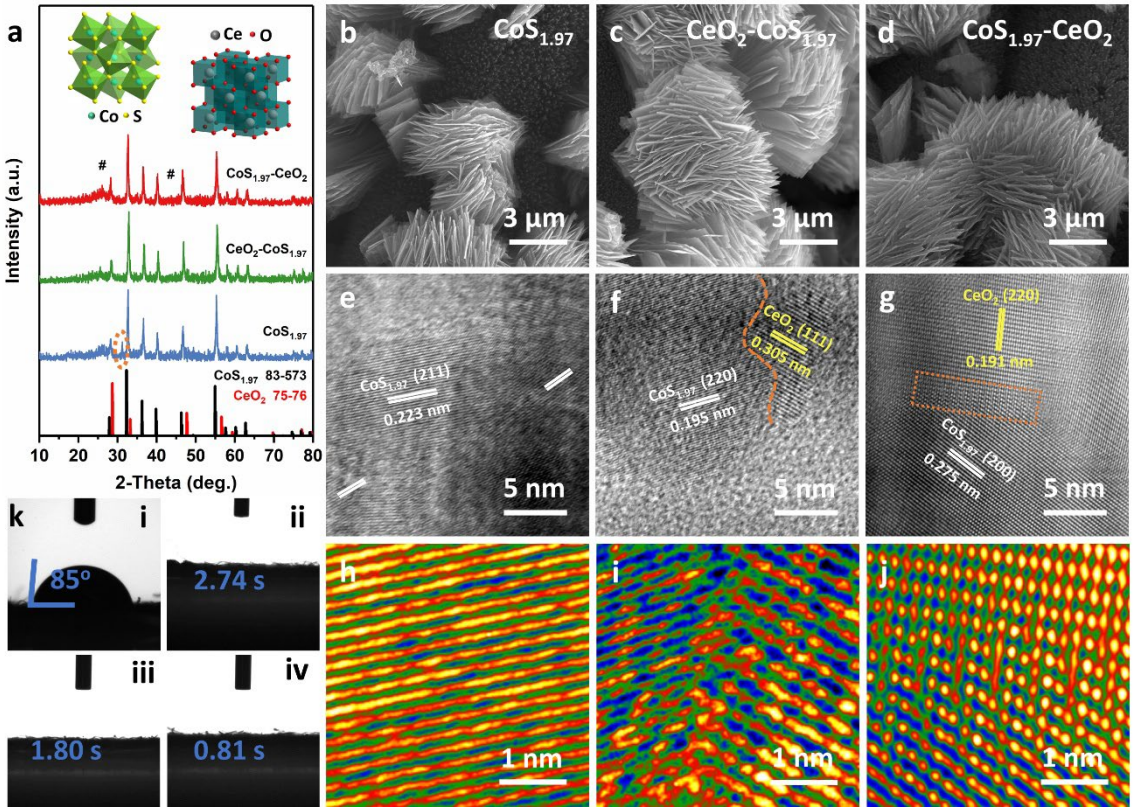

Figure 1. (a) XRD patterns of $CoS_{1.97}$, CeO_2-$CoS_{1.97}$ and $CoS_{1.97}$-CeO_2 (The "#" labels CFP substrate, "orange circle" labels the (220) plane diffraction peak of Co_3O_4 phase impurity). SEM images of (b) $CoS_{1.97}$, (c) CeO_2-$CoS_{1.97}$ and (d) $CoS_{1.97}$-CeO_2. HR-TEM images of (e) $CoS_{1.97}$, (f) CeO_2-$CoS_{1.97}$, (g) $CoS_{1.97}$-CeO_2. (h) The corresponding local enlarged drawing of $CoS_{1.97}$. Enlarged view at the interface of (i) CeO_2-$CoS_{1.97}$ and (j) $CoS_{1.97}$-CeO_2. (k) Wettability measurement of i) $CoS_{1.97}$, ii) CeO_2, iii) CeO_2-$CoS_{1.97}$ and iv) $CoS_{1.97}$-CeO_2 (inset "2.74 s", "1.80 s", "0.81 s" represent the time required for the droplet to fully spread after dripping).

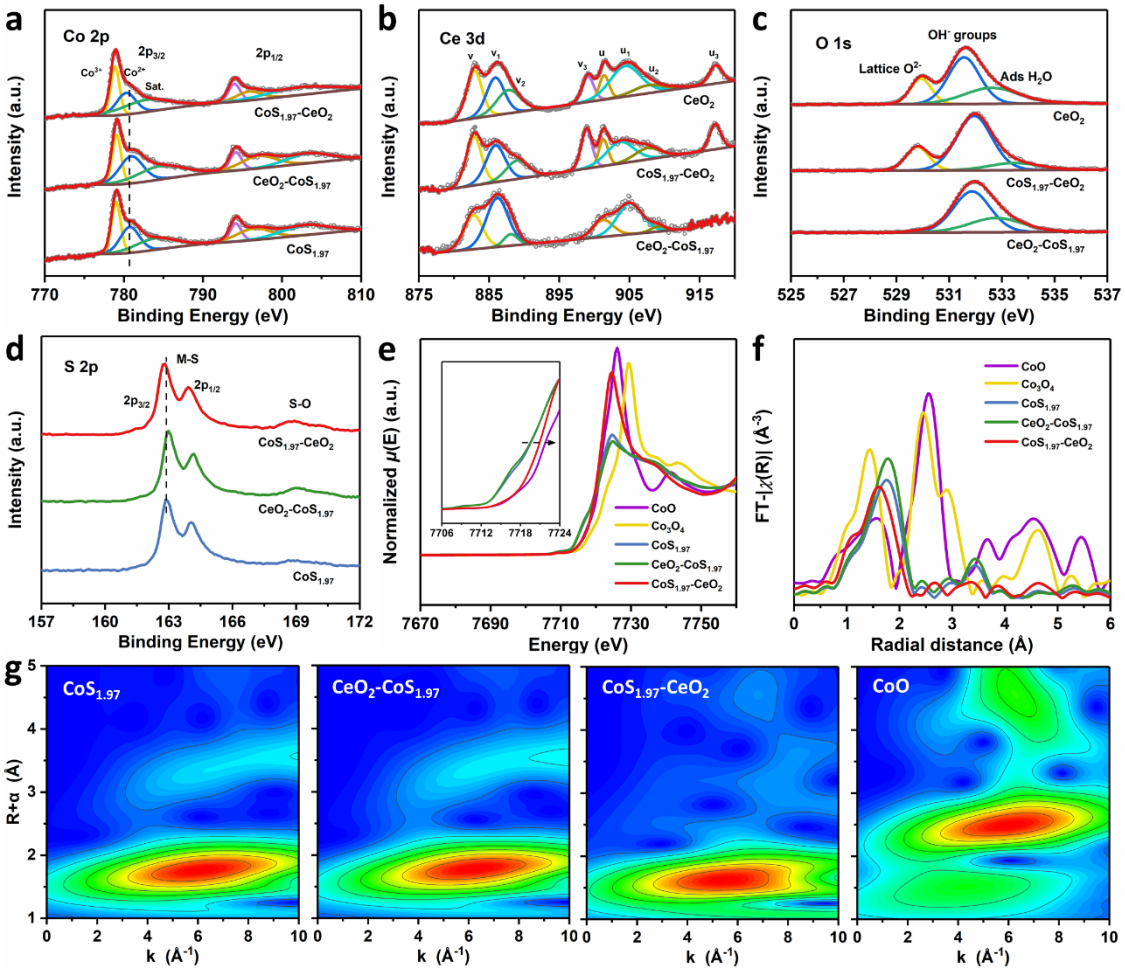

Figure 2. XPS spectra of (a) Co 2p and (d) S 2p for $CoS_{1.97}$, CeO_2-$CoS_{1.97}$, $CoS_{1.97}$-CeO_2. (b) Ce 3d and (c) O 1s for CeO_2-$CoS_{1.97}$, $CoS_{1.97}$-CeO_2, CeO_2. (e) Co K-edge XANES spectra for oxide standard samples and sulphides (inset shows the local enlarged drawing). (f) Co K-edge FT-EXAFS spectra in *R* space. (g) Corresponding EXAFS-CCWT images for $CoS_{1.97}$, CeO_2-$CoS_{1.97}$, $CoS_{1.97}$-CeO_2 and CoO.

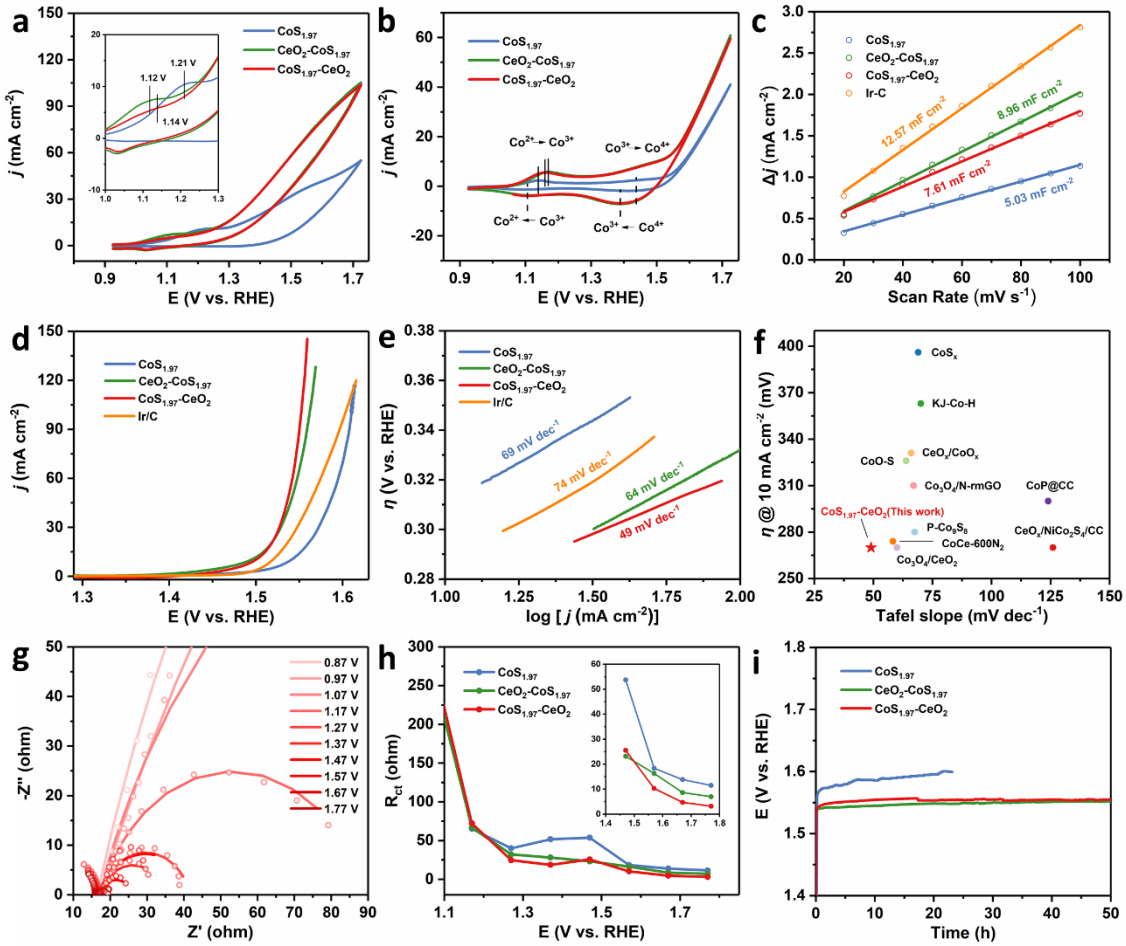

Figure 3. (a) The first cycle and (b) the 11th cycle CV for $CoS_{1.97}$, CeO_2-$CoS_{1.97}$, $CoS_{1.97}$-CeO_2 without iR-correction. (c) Capacitive currents as a function of scan rate for ECSA. (d) LSV polarization curves with 95% iR-correction. (e) Corresponding Tafel slope plots of $CoS_{1.97}$, CeO_2-$CoS_{1.97}$, $CoS_{1.97}$-CeO_2, commercial Ir/C catalyst. (f) Comparison of overpotentials at 10 mA cm^{-2} and Tafel slopes with the reported OER electrocatalysts. (g) Nyquist plots for $CoS_{1.97}$-CeO_2 at increasing applied potentials from 0.87 V (OCP) to 1.77 V (vs. RHE), the experimental data are marked with hollow circles, and the solid lines are the fitting lines. (h) Corresponding R_{ct} at the specific potential for $CoS_{1.97}$, CeO_2-$CoS_{1.97}$, $CoS_{1.97}$-CeO_2. (g) Long-term chronopotentiometry tests at 10 mA cm^{-2} in 1 M KOH.

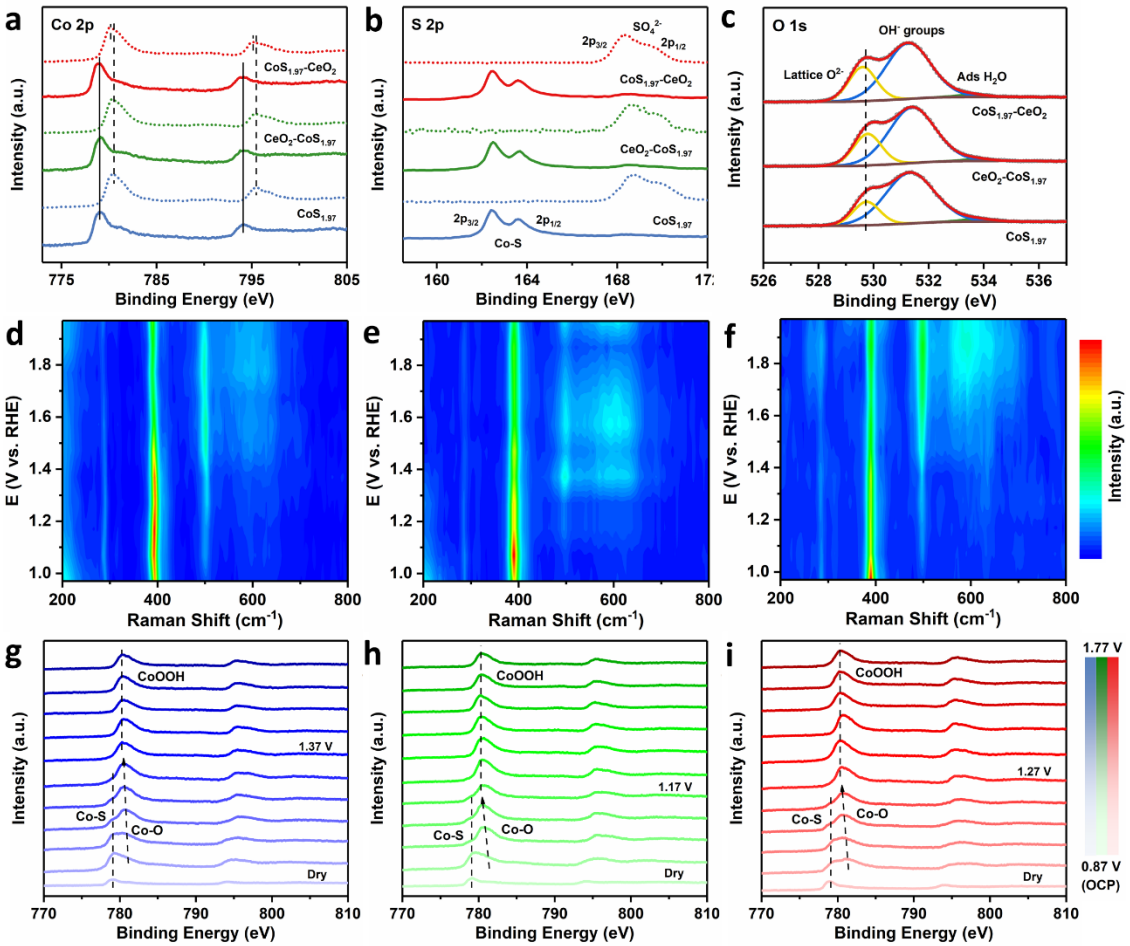

Figure 4. (a) Co 2p and (b) S 2p XPS spectra before (solid line) and after (dotted line) 10 h OER durability tests. (c) O 1s spectra after 10 h OER durability tests. Potential-dependent *in situ* Raman spectra of (d) $CoS_{1.97}$, (e) CeO_2-$CoS_{1.97}$, (f) $CoS_{1.97}$-CeO_2 from 0.97 V to 1.97 V (vs. RHE). *Quasi-operando* Co 2p XPS spectra for (g) $CoS_{1.97}$, (h) CeO_2-$CoS_{1.97}$, (i) $CoS_{1.97}$-CeO_2 at specific potential from 0.87 V (OCP) to 1.77 V (vs. RHE).

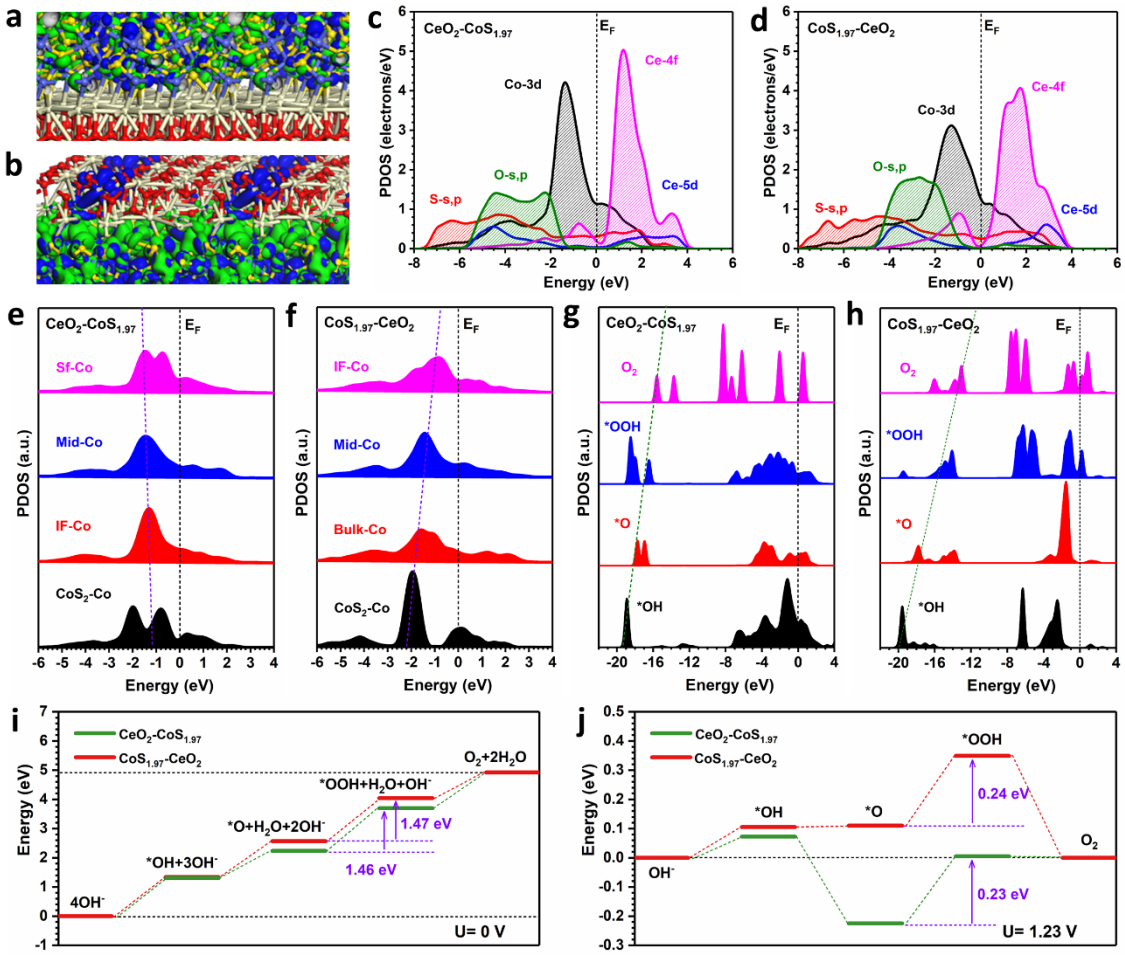

Figure 5. The 3D contour plot of electronic distribution near the Fermi level of (a) CeO_2-$CoS_{1.97}$ and (b) $CoS_{1.97}$-CeO_2. The PDOS of (c) CeO_2-$CoS_{1.97}$ and (d) $CoS_{1.97}$-CeO_2. The site-dependent PDOS of Co-3d in (e) CeO_2-$CoS_{1.97}$ and (f) $CoS_{1.97}$-CeO_2. The PDOS of key intermediates of (g) CeO_2-$CoS_{1.97}$ and (h) $CoS_{1.97}$-CeO_2. (i) The energetic pathway of OER in the alkaline environment. (j) The energetic pathway of OER in the alkaline environment under the applied potential of 1.23 eV.

Two novel $CeO_2/CoS_{1.97}$ heterostructure electrocatalysts (CeO_2-$CoS_{1.97}$ and $CoS_{1.97}$-CeO_2) are constructed to investigate the relationships between spatial architectures and OER performances, where different configuration endows hybrids with distinct intermediate adsorption, modulated electronic structures and promoted electrochemical reconstruction, thus improving the OER kinetics and performances. This work sheds light on the importance of rational design and synthesis of advanced hybrid electrocatalysts with functional spatial architectures.

Tengyuan Dai, Xin Zhang, Mingzi Sun, Bolong Huang,* Nan Zhang, Pengfei Da, Rui Yang, Zidong He, Wei Wang, Pinxian Xi, * and Chun-Hua Yan

Uncovering the Promotion of $CeO_2/CoS_{1.97}$ Heterostructure with Specific Spatial Architectures on Oxygen Evolution Reaction